70th International Astronautical Congress, Washington D.C., United States, 21-25 October 2019.

IAC-19,C1,6,4,x50894

ATTITUDE CONTROL FOR THE LUMIO CUBESAT IN DEEP SPACE

Á. Romero-Calvo,[1] J. D. Biggs, [1] F. Topputo[1]

The Lunar Meteoroid Impact Observer (LUMIO) is a 12U CubeSat designed to observe, quantify, and characterize the impact of meteoroids on the lunar surface. The combination of a highly demanding Concept of Operations (ConOps) and the characteristics of the deep-space environment determine the configuration of the spacecraft. This paper presents the preliminary Attitude Determination and Control System (ADCS) design of LUMIO, the reaction wheels desaturation strategy and Moon tracking control laws. The proposed solution is shown to (a) prevent the saturation of the reaction wheels, (b) minimize propellant consumption, (c) minimize the parasitic ΔV, (d) keep the pointing angle below a certain limit, and e) maximize power generation. Although no attempt is made to optimize the control parameters, the most efficient alternative in terms of propellant consumption is identified. The proposed LUMIO design could lay the foundations for a standardized minimum mass and volume ADCS system for CubeSats operating in deep-space.

Nomenclature

A Actual DCM matrix

A_d Desired DCM matrix

A_e Error DCM matrix

A_i Area of surface i

C_j Jacobi constant

$\vec{c}_{pi}$ Surface i position vector

c Speed of light

$\hat{\vec{d}}$ Disturbance estimation

$\vec{F}_i$ Solar pressure force in panel i

γ Thrusters tilting angle

$\vec{h}_r^d$ Desired angular momentum

$\vec{h}_r$ Angular momentum of the reaction wheels

$^\wedge$ Inverse hat map

h_{orbit} Altitude of the spacecraft

I Solar irradiance

$\vec{I}_{tot}$ Total impulse vector

J Generic inertia matrix

J_{depl} Inertia matrix for LUMIO's deployed configuration

J_{min} Minimization function

J_{pack} Inertia matrix for LUMIO's packed configuration

k_i Control parameters

l Distance between nozzles and Y-Z plane

m Number of thrusters

m_{SC} Mass of the spacecraft

$\mathcal{N}$ Matrix of thrust directions

$\vec{n}_s$ Unit vector normal to surface

Ω Aperture angle of a regular tetrahedron

$\odot$ Hadamard's product

P Solar constant

R Reaction wheels matrix

R_M Moon radius

ρ_d Diffusely reflected radiation

ρ_s Specularly reflected radiation

r Distance to the Sun

$\vec{S}$ Unit vector from Sun to surface

* Pseudo-inverse operator

^{s} Values after saturation

Δt_{MIB} Minimum Impulse Bit

$\mathcal{T}$ Torque matrix

θ Positive real number

$\vec{T}_{SRP}$ Solar radiation pressure torque

$\vec{t}$ Thrust vector

^{T} Transpose operator

$\dot{}$ Time derivative

$\vec{u}_{RW}$ Control momentum applied by the reaction wheels

$\vec{u}_c$ Control input

$\vec{u}_{des}$ Desired thrust torque

$\vec{u}_{lim}$ Thrust threshold

ΔV Spacecraft velocity increment

^{V} Skew-symmetric matrix or *hat map*

$\vec{\omega}$ Actual angular velocity

$\vec{\omega}_d$ Desired angular velocity

$\vec{\omega}_e$ Angular velocity error

[1]Department of Aerospace Science and Technology, Politecnico di Milano, Via Giuseppe La Masa, 34, 20156, Milan, Italy; alvaro.romero.calvo@gmail.com

X Body frame axis

$\vec{x}^M$ Normalized Moon pointing vector (J2000)

$\vec{x}^S$ Normalized Sun pointing vector (J2000)

x Distance between nozzles and X axis

x_i DCM unitary axis

Y Body frame axis

Y' Tilted body frame axis

Z Body frame axis

Z' Tilted body frame axis

Acronyms

ADCS	Attitude Determination and Control System.
CDR	Concurrent Design Review.
CMG	Control Moment Gyroscope.
CoM	Center of Mass.
ConOps	Concept of Operations.
DCM	Direction Cosine Matrix.
ESA	European Space Agency.
LUCE	LUnar CubeSat for Exploration.
LUMIO	Lunar Meteoroid Impact Observer.
MIB	Minimum Impulse Bit.
RW	Reaction Wheel.
SRP	Solar Radiation Pressure.
TLO	Top-Level Objectives.

1 Introduction

The last decade has witnessed a paradigm shift in the space sector due to the popularization of nanosatellites. Their appearance has democratized access to space, boosted the development of miniaturized technologies and extended the possibilities of distributed spacecraft architectures [1]. These new capabilities, mainly tested in low-Earth orbits, have also laid the foundations for the development of interplanetary nanosatellite missions such as Mars Cube One [2].

CubeSats are a standardized class of nanosatellites initially conceived as educational tools or technology demonstrators [3]. Their low cost, versatility and fast development time have led to their employment for actual scientific projects. Interplanetary missions may benefit from their scalability, modularity and distributed architecture to obtain redundant and more detailed scientific information [4]. Some examples of recently proposed interplanetary CubeSats are the University of Colorado's Earth Escape Explorer (CU-E3), the Cornell University Cislunar Explorers or the Fluid & Reason-LLC Team Miles [5].

The Lunar Meteoroid Impact Observer (LUMIO) is a 12U CubeSat mission to observe, quantify, and characterize the meteoroid impacts on the surface of the Moon by detecting their flashes on the lunar far-side. This complements the knowledge gathered by Earth-based observations of the lunar nearside, thus synthesizing a global information on the lunar meteoroid environment. LUMIO envisages a 12U CubeSat form-factor placed in a halo orbit at Earth-Moon L2 to characterize the lunar meteoroid flux by detecting the impact flashes produced on the far-side of the Moon. The mission employs the LUMIO-Cam, an optical instrument capable of detecting light flashes in the visible spectrum [6]. LUMIO is one of the two winners of ESA's LUnar CubeSat for Exploration (LUCE) SysNova competition, and as such it is being considered by ESA for implementation in the near future.

One of the major challenges of the mission is the strict pointing budget, which imposes high-precision tracking of a specific attitude that maximizes power generation. This is particularly relevant for the Attitude Determination and Control System (ADCS) due to the limited capacity of the reaction wheels. In addition, the de-tumbling and de-saturation maneuvers are undertaken using only four thrusters, which adds to the complexity of the control design.

This paper describes the attitude control strategy for the LUMIO mission focusing on the configuration design of the reaction wheels and thruster-based de-saturation. Due to the tight constraint on the maximum momentum storage, the placement of the reaction wheels significantly affects the desaturation strategy and requires optimization. Different desaturation strategies are presented which require an unconventional approach to their design due to the employment of only four thrusters.

The work is organized as follows: Sec. 2 summarizes the mission and its most relevant characteristics for the ADCS subsystem, whose configuration is discussed in Sec. 3 and control laws in Sec. 4. The performance of different reaction wheel configurations and desaturation strategies is analyzed in Sec. 5. Finally, the conclusions and potential future developments are presented in Sec. 6.

2 Mission Overview

2.1 Top-Level Objectives (TLO)

The LUMIO mission aims to characterize the flux, magnitude, luminous energy, and size of the meteoroids impacting the lunar farside. This would help advance the understanding of how meteoroids evolve in the cislunar space and complement the existing observations of the lunar nearside. From the technological perspective, the mission wants to demonstrate the deployment and autonomous operation of a CubeSat in the lunar environment [7]. Those goals are summarized in the TLO listed in Tab. 2.

2.2 Concept of Operations (ConOps)

In the Circular Restricted Three-Body Problem, the libration points are at rest with respect to a frame co-rotating with the smaller and larger primaries. Consequently, a halo orbiting the Earth–Moon L2 always faces the lunar farside. On top of this, for a wide range of Jacobi energies, Earth–Moon L2 halos are almost locked into a 2:1 resonance, that is 2 orbital revolutions in 1 synodic period $T_{syn} = 29.4873$ days.

Tab. 2: Top-Level Objectives of LUMIO [7].

ID	Objective
01	To perform remote sensing of the lunar surface and measurement of astronomical observations not achievable by past, current, or planned lunar missions
02	To demonstrate deployment and autonomous operation of CubeSats in lunar environment, including localization and navigation aspects
03	To demonstrate miniaturization of optical instrumentation and associate technology in lunar environment
04	To perform inter-satellite link to a larger Lunar Communications Orbiter for relay of data and for TT&C
05	To demonstrate CubeSat trajectory control capabilities into lunar environment
06	To gain European flight heritage in emplacing and operating assets at Earth-Moon Lagrange points

The quasi resonance locking, which is also preserved in the full ephemeris quasi-halos, enables LUMIO operations to be steady, repetitive, and regular. Within the operative phase, each synodic month LUMIO moves along a) a Science orbit (dark solid line in Fig. 1) and b) a Navigation and Engineering orbit (light colored solid line in Fig. 1). During the Science orbit, lasting approximately 14 days, the Moon farside has optimal illumination conditions to perform flash observations (i.e., at least half lunar disk is dark). On the other hand, during the Nav&Eng orbit the Moon farside illumination conditions are apt to optical navigation routines. In this way, LUMIO preliminary ConOps is somewhat simplified and tight to both resonance mechanisms and illumination conditions to properly enable scientific or other operations.

2.3 ADCS requirements

LUMIO ConOps determine the design of the ADCS, whose high-level requirements are summarized in Tab. 3. The entries 03 to 05 have a special relevance in the context of this work. During the science and navigation phases the spacecraft has to point the Moon to enable full disk coverage (03). In the former case, this requirement arises from the need of visualizing the impacts of meteoroids, while in the later it is determined by the visual navigation algorithms. If one axis is fixed, the second degree of freedom in the attitude is determined by power generation (04). In addition, the input power is maximized by allowing a rotation of the solar arrays around their axis. A certain pointing stabilization (05) is required to avoid blurred images and enable flash detection with the LUMIO Camera. Requirements 01, 02 and 06 are common in ADCS design, the last arising from operational range of the star tracker.

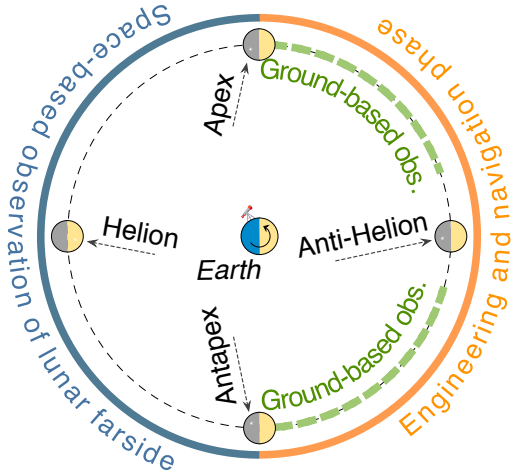

Fig. 1: LUMIO Concept of Operations [8].

Tab. 3: LUMIO ADCS high-level requirements [7].

ID	Name	Requirement
01	De-Tumbling	After the separation from the Lunar Orbiter, the ADCS is required to de-tumble the spacecraft from tip-off rates of, up to, 30 deg/s in each axis.
02	Initialization	Maneuver the solar panels to a power safe mode within a time compatible with the electrical energy capability.
03	Moon Pointing	The ADCS is required to point with an accuracy of less than 0.1 deg during the science and navigation phases.
04	Power Maximization	The attitude is required to maximize the power generation capability of the solar panels given the Moon pointing (halo and part of the transfer) constraint and the Earth pointing (parking) constraint.
05	Pointing Stabilization	The ADCS is required to provide a minimum pointing stabilization of 79.90 arcsec/s during the science phase.
06	Slew Rate	The ADCS shall provide a maximum slew rate of 1 deg/s.

2.4 ADCS hardware

The preliminary list of ADCS hardware was defined in the Phase A design of LUMIO. During the Concurrent Design Review (CDR) performed at the European Space Agency (ESA) Concurrent Design Facility [9] it was decided to update the hardware components with the ones listed in Tab. 4. The sizing and model selection of the reaction wheels and the orientation of thrusters depend on the desaturation strategy, and are hence the main outcomes of this work.

3 ADCS Configuration

3.1 Deep space environment

The deep space environment presents unique characteristics that result in specific ADCS architectures. The absence of relevant magnetic fields in lunar orbit discards any

Tab. 4: LUMIO ADCS hardware list

Component	Qty.	Model
Sun Sensor	2	SolarMEMS nanoSSOC-D60
Star Tracker	2	Hyperion ST400
IMU	1	Sensonor STIM 300
Thruster	4	Aerojet MPS-130
RW	3	See Sec. 3.5

magnetorquer-based desaturation procedure. A dedicated ADCS propulsion system or a careful management of Solar Radiation Pressure (SRP) torques is then required to desaturate the momentum management devices. In the case of LUMIO, the strict requirement ADCS-03 discards the second option, and hence a set of dedicated ADCS thrusters must be installed.

Given the large orbit altitude, the reflected radiation coming from the surface is negligible and the major disturbance to be considered is the SRP. Internal disturbances such as the mechanical oscillations of the solar arrays or liquid sloshing have only a short-term effect and, nevertheless, cannot be faithfully simulated in such an early design phase.

3.2 Inertial properties

The inertia matrix, Center of Mass (CoM) position and principal axes of inertia were computed with a block model developed in CATIA V5 6R-2018. The mass of each block was assigned according to the preliminary mass budget (which totals 22.82 kg) and distribution of hardware components. Fig. 2 depicts the deployed and packed inertial Catia models with the corresponding blocks.

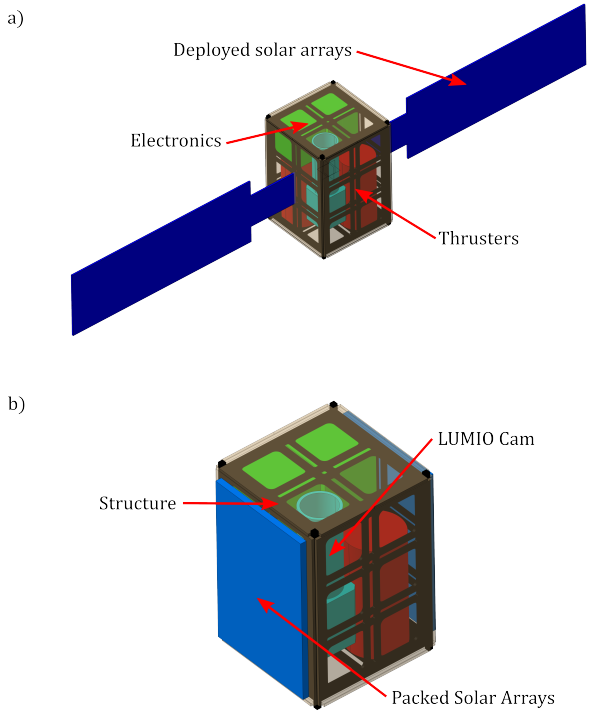

Fig. 2: Catia inertial modeling for (a) LUMIO's deployed configuration, and (b) LUMIO's packed configuration.

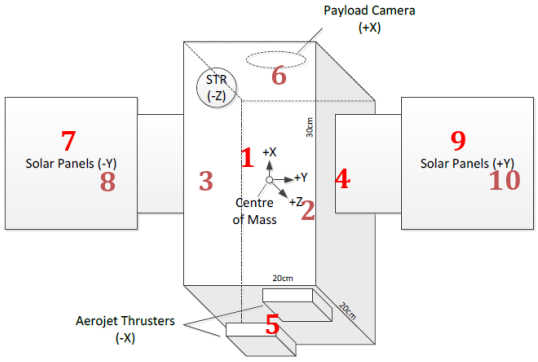

Fig. 3: LUMIO's Body Frame and surface numbering; adapted from [10].

The simulation returned a maximum deviation between the principal inertial and geometrical axes of symmetry of 11°. The maximum displacement of the CoM from the geometrical center was of 1.6 cm. Since these computations correspond to a preliminary state of the design, it was decided to identify the principal axes of inertia with the geometric ones and estimate the effect of SRP in a worst case scenario with the CoM displaced 1.6 cm in the axis of the solar arrays (Y). The body reference system represented in Fig. 3 is considered in this work. Under these assumptions, the principal inertia matrices for the packed and deployed configurations are

$$J_{pack} = \begin{bmatrix} 30.5 & 0 & 0 \\ 0 & 20.9 & 0 \\ 0 & 0 & 27.1 \end{bmatrix} \times 10^{-2} \text{ [kg m}^2\text{]}, \quad (1)$$

$$J_{depl} = \begin{bmatrix} 100.9 & 0 & 0 \\ 0 & 25.1 & 0 \\ 0 & 0 & 91.6 \end{bmatrix} \times 10^{-2} \text{ [kg m}^2\text{]}. \quad (2)$$

3.3 Target reference frame

The Earth–Moon L2 quasi-halo orbit with a $C_j = 3.09$ Jacobi constant is the baseline operational scenario for LUMIO [11]. The desired attitude is calculated from a predefined SPICE kernel by applying the reference frame definition

$$A_d = \begin{bmatrix} \vec{x}_1 = \vec{x}^M \\ \vec{x}_2 = \dfrac{\vec{x}^S \times \vec{x}_1}{|\vec{x}^S \times \vec{x}_1|} \\ \vec{x}_3 = \dfrac{\vec{x}_1 \times \vec{x}_2}{|\vec{x}_1 \times \vec{x}_2|} \end{bmatrix}, \quad (3)$$

where $\vec{x}^M$ and $\vec{x}^S$ denote the normalized Moon and Sun pointing vectors in the inertial reference frame J2000. It can be shown that this reference frame maximizes power generation by allowing the solar arrays to be always normal to the Sun vector [6].

The angular velocity $\vec{w}_d$ and its derivative $\dot{\vec{w}}_d$ are computed numerically by making use of the Direction Cosine Matrix (DCM) Kinematic Differential Equation

$$\vec{\omega}_d^V = -\frac{\mathrm{d}A_d}{\mathrm{d}t} A_d^T, \quad (4)$$

with A_d being the desired DCM from the J2000 inertial to the body reference frames and the superscript "V" denoting

the skew-symmetric matrix or *hat map*, defined for the case of $\vec{w}$ as

$$\vec{\omega}^V = \begin{bmatrix} 0 & -\omega_3 & \omega_2 \\ \omega_3 & 0 & -\omega_1 \\ -\omega_2 & \omega_1 & 0 \end{bmatrix}. \quad (5)$$

The actual DCM matrix is named as A in this work.

3.4 Solar Radiation Pressure

The intensity of solar radiation at Earth's orbit is approximately 1366.1 W/m^2. Considering a mean distance to Sun of 149.6×10^6 km, the inverse power law becomes

$$I = \frac{P}{4\pi r^2}, \quad (6)$$

I being the total solar irradiance in W/m^2, $P \approx 3.842 \times 10^{26}$ W the solar constant and r the distance to Sun. The distance between LUMIO and the moon oscillates between 4×10^4 km and 9×10^4 km, so the Lunar radiation pressure can be safely neglected, as at 100 km altitude it already represents a 20% of solar radiation pressure [12].

The force exerted by SRP on a flat, Lambertian surface is given by [13]

$$\vec{F_i} = \frac{I}{c} A_i (\vec{S} \cdot \vec{n}_{si}) \left\{ (1-\rho_s)\vec{S} + \left[2\rho_s (\vec{S} \cdot \vec{n}_{si}) + \frac{2}{3}\rho_d \right] \vec{n}_{si} \right\}, \quad (7)$$

where c is the speed of light, A is the surface area, $\vec{S}$ is the unit vector pointing from the Sun to the surface, $\vec{n}_s$ is a unit vector normal to the surface (and directed towards the interior), and $\rho_s = 0.6$ and $\rho_d = 0.1$ are the specularly and diffusely reflected radiation. The vectors are expressed in the body frame.

The SRP torque is computed with a simplified model that neglects the interaction between different surfaces (shadows, reflections). The result is

$$\vec{T}_{SRP} = \sum_{i=1}^{n} \vec{c}_{pi} \times \vec{F}_i \quad \text{if} \quad \vec{S} \cdot \vec{n}_{si} > 0, \ \vec{0} \text{ otherwise}, \quad (8)$$

with $\vec{c}_{pi}$ being the position vectors between the center of mass of the spacecraft and the center of pressure of the surfaces, assumed to be the same as their geometrical centers. If the spacecraft is eclipsed, the torque is set to zero. The eclipse, without making distinctions between umbra and penumbra, is produced when

$$\vec{x}^M \cdot \vec{x}^S \leq \frac{R_M + h_{orbit}}{\sqrt{R_M^2 + (R_M + h_{orbit})^2}}, \quad (9)$$

where R_M is the radius of the Moon and h_{orbit} is the altitude of the spacecraft. The surfaces of LUMIO are numbered according to Fig. 3, and correspond to the columns of

$$n_s = \begin{bmatrix} 0 & 0 & 0 & 0 & 1 & -1 & \sin\alpha & -\sin\alpha & \sin\alpha & -\sin\alpha \\ 0 & 0 & 1 & -1 & 0 & 0 & 0 & 0 & 0 & 0 \\ 1 & -1 & 0 & 0 & 0 & 0 & \cos\alpha & -\cos\alpha & \cos\alpha & -\cos\alpha \end{bmatrix} \quad (10)$$

$$c_p = \begin{bmatrix} 0 & 0 & 0 & 0 & -10 & 10 & 0 & 0 & 0 & 0 \\ 0 & 0 & -10 & 10 & 0 & 0 & -45 & -45 & 45 & 45 \\ -10 & 10 & 0 & 0 & 0 & 0 & 0 & 0 & 0 & 0 \end{bmatrix} - \begin{bmatrix} 0 \\ 1.6 \\ 0 \end{bmatrix} \text{ [cm]},$$

$$A = \begin{bmatrix} 6 & 6 & 6 & 6 & 4 & 4 & 12 & 12 & 12 & 12 \end{bmatrix} \times 10^{-2} \text{ [m}^2\text{]},$$

where α is the rotation angle of the solar panels, set to maximize the product $(\vec{S} \cdot \vec{n}_{si})$. In the target reference frame, where the second base vector approximately points to the Sun, it is possible to align $\vec{S}$ and $\vec{n}_{si}$ with a rotation of the solar panels around their axis.

3.5 Reaction wheels configuration

A fundamental process when implementing a set of momentum management devices is defining their optimum arrangement. The optimization goal can be the minimization of the torque requirements (or, equivalently, power demand) or the optimization of the momentum/torque envelope or workspace size. This problem has historically raised significantly less attention than the development of ADCS control laws [14]. In [15] it is shown that a tilt angle of arctan(1/2) in a pyramidal single gimbal Control Moment Gyroscope (CMG) system generates a spherical momentum workspace. The maximum momentum and torque envelopes are computed in [16] for four dissimilar reaction wheels. The influence of the tilt angle of a pyramidal configuration on power consumption is studied in [14] for a specific maneuver. In [17] several 3-axis and 4-axis arrangements are simulated in the same scenario and the ones with a minimum total torque level are identified. An interesting approach to the problem is presented in [18], where an optimization procedure is given to obtain the orientations R and momentum bias for a set of three identical reaction wheels subjected to momentum, torque and power constraints.

The previous works highlight that the optimum arrangement is mission-dependent. In the case of LUMIO, a major importance has been given to increasing the period between desaturation maneuvers (i.e., optimizing the angular momentum capacity for the mission profile). This choice aims to reduce the effects that those maneuvers would cause in the normal operation of the spacecraft. A more common goal is the reduction of maximum power consumption (or maximum torque), but a significant minimum value is required in any case to compensate the ADCS thrusters torque during desaturation. For other situations, the power requirements can be lowered by performing slower maneuvers. The analysis of alternatives is given in Sec. 5.

3.6 Reaction wheels control

The equations of attitude motion of a spacecraft with reaction wheels are given by [19]

$$J\dot{\vec{\omega}} + \vec{\omega} \times J\vec{\omega} = \vec{u}_{RW} + \vec{T}_{SRP}, \quad (11)$$

$$\dot{\vec{h}}_r = -R^*(\vec{u}_c + \vec{\omega} \times R\vec{h}_r), \quad (12)$$

$$\vec{u}_{RW} = -A\dot{\vec{h}}_r^s - \vec{\omega} \times R\vec{h}_r^s, \quad (13)$$

where $\vec{u}_{RW}$ is the control momentum applied by the reaction wheels, $\vec{u}_c$ is the control input, $\vec{h}_r$ is the angular momentum of the reaction wheels, R is the actuators matrix (where each column represents the axis of rotation of each wheel) and the superscript " $*$ " denotes the pseudo-inverse. This model allows imposing a limitation on the maximum angular

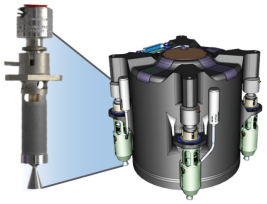

Throughput Capability (each):	3.0 kg
Pulses:	10,000
Total Impulse Capability (each):	6,000 N-s
MIB:	0.0004 N-s
Thrust:	.25 - 1.25 N
Isp:	206 - 235 sec

Fig. 4: Aerojet MPS-130 main specifications and 1U version representation; adapted from Aerojet MPS-130 datasheet.

momentum and torque, with the superscript "s" referring to the values after saturation.

3.7 Thrusters configuration

Two 2U versions of the Aerojet MPS-130 were selected at the ESA CDR as the baseline propulsion system [10]. Its preliminary design and main specifications are given in Fig. 4.

The location of both modules is given in Fig. 5. In order to enable a 3-axis control, the nozzles, directed towards the $-X$ axis, are tilted an angle $\gamma = 10^\circ$ in the direction of the green arrows. A minimum torque of 6.3 mNm in the Y' and Z' axes is achieved with this configuration. At the time of writing it is unclear if each thruster is throttleable in the range 0.0625-0.3125 N or if the thrust value is set before launch. In the former case, lower torque values would be achieved by firing the opposite thrusters. If the reaction wheels provide higher torque values, a static desaturation strategy can be considered (i.e., the reaction wheels could be desaturated without producing an off-pointing of the satellite).

The shift of the CoM is not a major concern for this configuration. At the beginning of the science mission a ΔV of 25.9 m/s will remain from the initially allocated 195.5 m/s [10]. According to the Aerojet MPS-130 datasheet, that would correspond to approximately 371 g of usable propellant. In a worst case scenario, its consumption would produce a position shift of +3 mm in the X direction for a initial mass of 20 kg, which has little effect on the torque matrix. The

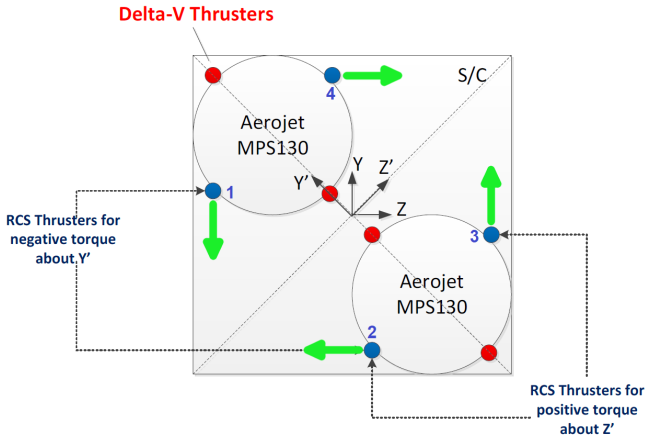

Fig. 5: Thrusters configuration. The green arrows represent the tilting directions of the ADCS thrusters; adapted from [10].

reader should note that the Aerojet MPS-130 engine stores its propellant in glass state and employs a piston to remove sloshing [20]. Once measured, the CoM position would then be subjected to a small uncertainty solely dependent on fuel consumption.

3.8 Thrusters control

The ADCS thrusters control strategy aims to map a desired torque value $\vec{u}_{des}$ to the actual thrust vector $\vec{t}$, where each row corresponds to one thruster. A discrete projective control is firstly evaluated. It imposes a constant thrust level ($t = 0.0625$ N) and calculates the combination of on/off states that best follows the desired control for each time step. This combination minimizes the function

$$J^n_{min} = ||\vec{u}_{des} - \vec{u}_n||, \text{ with } \vec{u}_n = \mathcal{T}\vec{t} \tag{14}$$

where n identifies one of the 16 possible combinations of 4 thrusters, $\mathcal{T}$ is the torque matrix and each element of $\vec{t}$ is either 0 or 0.0625 N. The torque matrix for a tilting of $\gamma \approx 10^\circ$ is computed easily after noticing that the nozzles rest approximately in the X-Y and X-Z planes. Therefore:

$$\mathcal{T} = \begin{bmatrix} x\sin\gamma & -x\sin\gamma & x\sin\gamma & -x\sin\gamma \\ -x\cos\gamma & l\sin\gamma & x\cos\gamma & -l\sin\gamma \\ -l\sin\gamma & x\cos\gamma & l\sin\gamma & -x\cos\gamma \end{bmatrix}, \tag{15}$$

where $x = 0.09$ m is the distance between the nozzles and the X axis and $l = 0.15$ m is the distance to the Y-Z plane. A thrust threshold is set as $\vec{u}_{lim} = [2, 3.9, 3.9]^T$ mNm, corresponding to the minimum possible compensated torque on each axis. If $|u_{des,i}|$ is below $k_4\vec{u}_{lim}$, it is set to 0, while if it is between $k_4\vec{u}_{lim}$ and $\vec{u}_{lim}$ it is set to $\vec{u}_{lim}$. k_4 is a tuning parameter that controls the sensitivity of the propulsion system. If k_4 is close to 0, a higher pointing accuracy will be achieved with a higher propellant consumption, while if it is close to 1 the second is minimized at the expenses of pointing accuracy. It should be noted that the axes Y and Z are coupled since the torque uncoupling is produced in the Y' and Z' axes. Also, that the generation of torque will lead in any case to a parasitic ΔV in the X axis.

The projective control assumes that a single thrust level is available for each thruster. This strategy may be improved if a range of thrust values is allowed for each thruster. Unfortunately, it was not possible to determine if the Aerojet MPS-130 thrusters have such capability. If that was the case, a constrained optimal control problem could be formulated with the objective of minimizing the total thrust function

$$J_{min} = \sum_{i}^{m=4} t_i \tag{16}$$

subjected to $\mathcal{T}\vec{t} = \vec{u}_{des}$ and $t_i > 0$ N. In this case, t_i ranges from 0.0625 to 0.3125 N. The output should then be corrected to impose $t_i \in [0.0625, 0.3125]$ N, in such a way that the control value is limited to 0.3125 N, while if it drops below $k_4 u_{min}$ it is set to 0. Again, the range between $k_4 u_{min}$ and u_{min} is set to u_{min}.

The previous strategy can be implemented through a standard linear solver or, more efficiently, by following the

procedure described in [21]. According to its Theorem 1, given any targeted $\vec{u}_{des}$ torque, the vector of thrust values can be computed as

$$\vec{t} = \mathcal{T}^{+}\vec{u}_{des} + \theta\vec{\omega}, \tag{17}$$

with $\mathcal{T}^{+} = \mathcal{T}^{T}(\mathcal{T}\mathcal{T}^{T})^{-1}$ and $\vec{\omega} > \vec{0}$ being the Moore-Penrose pseudoinverse and the kernel (null-space) of $\mathcal{T}$, respectively, and $\theta > max_{i=1,\dots,m}(-A^{+}\mathcal{T})_i/w_i$ being a positive real number that ensures that $t_i \geq \vec{0}$. In order to activate the thrusters when a minimum thrust limit is set, the minimum thrust value 0.0625 N can be added to θ.

The Minimum Impulse Bit (MIB) of the thrusters is $\Delta t_{MIB} = 0.0064$. This lower limit is respected in the simulations carried out in Sec. 5 by imposing a lower time step limit for the variable time solver.

3.9 Parasitic ΔV

The parasitic vectorial $\Delta\vec{V}$ is given by

$$\Delta\vec{V}_{par} = \frac{\mathcal{N}}{m_{SC}}\vec{I}_{tot}, \tag{18}$$

where $\vec{I}_{tot}$ is the total impulse produced by each thruster, $\mathcal{N}$ the matrix of thrust directions and $m_{SC} = 22.82$ kg is the mass of the spacecraft. The matrix $\mathcal{N}$ is given by

$$\mathcal{N} = \begin{bmatrix} \cos\gamma\cos\gamma & \cos\gamma & \cos\gamma \\ \sin\gamma & 0 & -\sin\gamma & 0 \\ 0 & \sin\gamma & 0 & -\sin\gamma \end{bmatrix}. \tag{19}$$

This vectorial formulation has the advantage of showing specific information in the body axes, an useful knowledge for optimizing the station-keeping maneuver.

4 Control laws

The attitude control laws for Moon tracking and simultaneous desaturation and tracking are given in this section, while the stability proofs for both are detailed in the Appendix A.

4.1 Moon tracking control law

A possible Lyapunov-stable tracking control law in the presence of SRP disturbances would be given by [22, 23]

$$\begin{aligned}\vec{u} = &-k_1\vec{\omega}_e - k_2(A_e^T - A_e)^V + \vec{\omega}\times J\vec{\omega} \\ &+ J(A_e\dot{\vec{\omega}}_d - [\vec{\omega}_e]^{\wedge}A_e\vec{\omega}_d) - \hat{\vec{d}},\end{aligned} \tag{20}$$

with k_i being the control tuning parameters, $\vec{\omega}_e = \vec{\omega} - A_e\vec{\omega}_d$ the angular velocity error, $A_e = AA_d^T$ the error DCM matrix and $\hat{\vec{d}}$ the disturbances estimation, equal in this case to the SRP disturbance described in Sec. 3.4. The superscript $^{\wedge}$ denotes the inverse hat map. The application of this control law consequently ensures the satisfaction of the requirement ADCS-03 during the science and navigation phases.

4.2 Desaturation and tracking control law

In order to desaturate the reaction wheels, a control algorithm must a) reduce their angular momentum to a safe value, and b) simultaneously fire the spacecraft thrusters to continue tracking the Moon and satisfy the requirement ADCS-03 during desaturation. The ideal tracking law given in Eq. (20) is then augmented and linked to the ADCS thrusters, while a new law of the form

$$\vec{u}_c = k_3 R(\vec{h}_r - \text{sign}(\vec{h}_r^T)\odot\vec{h}_r^d) - \vec{\omega}\times R\vec{h}_r, \tag{21}$$

where k_3 is the control parameter, h_r^d is the desired angular momentum, and " $\odot$ " refers to Hadamard's product, asymptotically stabilizes the reaction wheels spin. The multiplication of the desired angular momentum vector by the sign of the actual momentum of the reaction wheels aims to avoid an unwinding behavior. This expression can also be used to control the thrusters in a zero-sum strategy, but as their operation is not continuous that would derive in an off-pointing of the satellite.

The tracking control law must finally be followed by the ADCS thrusters and include the control torque given by Eq. (21) as an external disturbance, resulting in

$$\begin{aligned}\vec{u} = &-k_1\vec{\omega}_e - k_2(A_e^T - A_e)^V + \vec{\omega}\times J\vec{\omega} \\ &+ J(A_e\dot{\vec{\omega}}_d - [\vec{\omega}_e]^{\wedge}A_e\vec{\omega}_d) - \hat{\vec{d}} - \vec{u}_c.\end{aligned} \tag{22}$$

5 Results and discussion

5.1 Reaction wheels configuration

The Moon tracking has to be ensured by the ADCS while the spacecraft is subjected to external disturbance torques. The most important of them is the SRP, which follows a repetitive oscillatory track in the $X - Z$ body axes throughout the mission. This behavior is depicted in Fig. 6 and is consistent with the L2 halo 2:1 resonance (see Sec. 2.2).

The control load should be equally distributed among the reaction wheels in order to extend the period between desaturation maneuvers. This discards any configuration on which a single reaction wheel is aligned with the directions $[\pm1, \pm1, 0]$, that correspond to the maximum control torque requirement. Two options are here studied. The first is the basic 3-axis configuration, while the second is a *Regular Tetrahedron* around the X axis where one of the wheels lies in the X-Z plane. The aperture of the tetrahedron with respect to the symmetry axis is set to $\Omega = 60^{\circ}$. The corresponding R matrices are

Tab. 5: Proposed reaction wheels for LUMIO. Last column reports the mass saving with respect to the heaviest option.

ID	$\vec{h}_r^{max}$ (mNms)	$\dot{\vec{h}}_r^{max}$ (mNm)	m (g)	Δm (g)
Hyperion RW400 1	15	8	155	-675
GOMspace GSW600	19	2	180	-600
Hyperion RW400 2	30	8	210	-510
Hyperion RW400 3	50	8	380	0

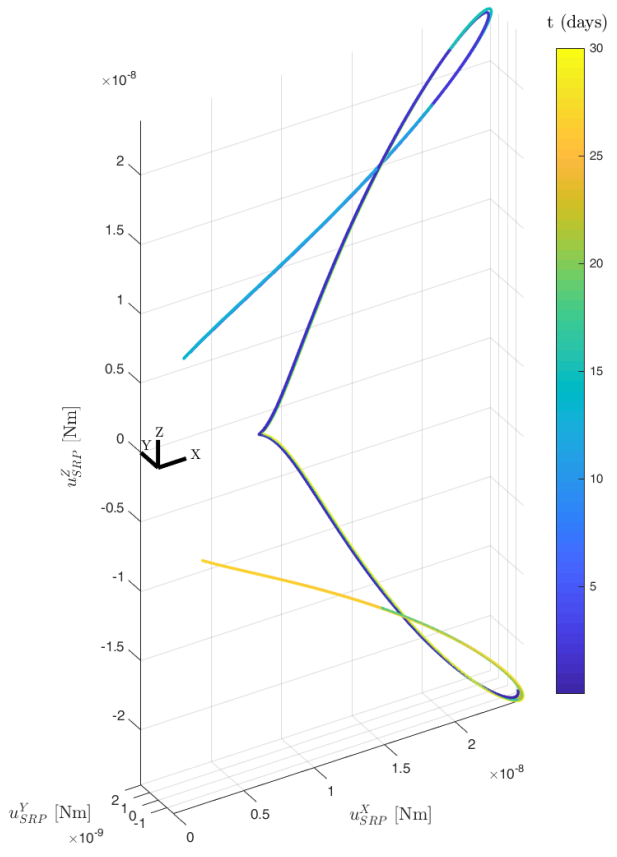

Fig. 6: SRP torque in the body frame during the first 30 days of mission.

$$R_b = \begin{bmatrix} 1\,0\,0 \\ 0\,1\,0 \\ 0\,0\,1 \end{bmatrix}, \; R_t = \begin{bmatrix} \cos\Omega & \dfrac{\cos\Omega}{\sqrt{1+\cos^2\Omega}} & \dfrac{\cos\Omega}{\sqrt{1+\cos^2\Omega}} \\ 0 & \dfrac{-\sqrt{3}/2}{\sqrt{1+\cos^2\Omega}} & \dfrac{\sqrt{3}/2}{\sqrt{1+\cos^2\Omega}} \\ \sin\Omega & \dfrac{-1/2}{\sqrt{1+\cos^2\Omega}} & \dfrac{-1/2}{\sqrt{1+\cos^2\Omega}} \end{bmatrix}. \tag{23}$$

The reaction wheels listed in Tab. 5 are subsequently considered. The objective is to select the technology that ensures a desaturation-free period of at least 15 days without increasing unnecessarily the mass of the vehicle. The first 30 days of mission are simulated in Figs. 7 and 8 with the two proposed RWs configurations. The torque requirements are extremely low in both cases, although slightly higher in the basic configuration. The angular momentum evolution is qualitatively similar with only small differences in the maximum values. Both configurations can avoid the desaturation maneuver during 15 days with almost all the RW models. However, since the wheels are close to saturation after two weeks and a simplified SRP model was employed, it was decided to implement the Hyperion RW400 2 set with respective maximum angular momentum and torque of 30 mNms and 8 mNm. The 30 days evolution of the angular momentum is smoother with the 60° tetrahedron configuration, which will be subsequently considered.

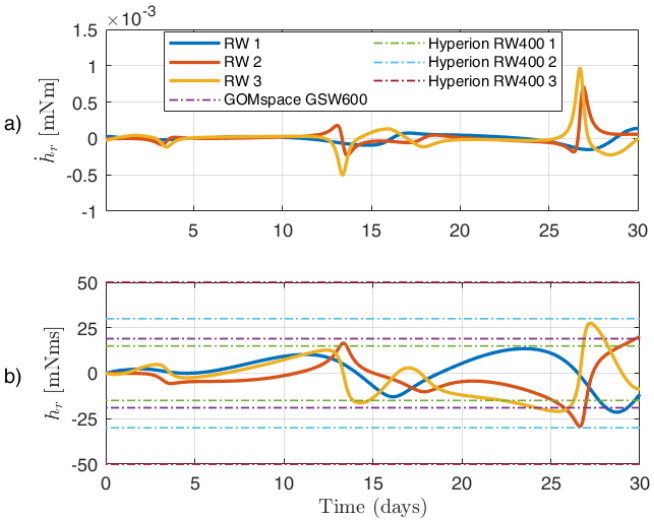

Fig. 7: a) Torque and b) angular momentum for the Cartesian RWs configuration during the first 30 days in the operational orbit.

5.2 Rigid desaturation schedule

The science phase of LUMIO lasts approximately 14 days. A rigid desaturation schedule is here considered by imposing desaturation maneuvers at days -1 and 15 of the resonant orbit. This choice leaves the science and engineering orbits completely free of disturbances, but does not minimize the number of maneuvers.

Simulations cover the first year of the mission and implement the models described in Secs. 3 and 4 with the deployed matrix configuration given in Sec. 3.2. The projective thrusters control is first evaluated with parameters $k_1 = 0.0005$, $k_2 = 0.0005$, $k_3 = 0.01$ and $k_4 = 0.5$. The tracking algorithm was assumed by the propulsion system during desaturation, imposing $k_1 = 100$ and $k_2 = 100$. The RWs desaturation control k_3 cannot be increased without obtaining a larger pointing deviation since the thrusters are

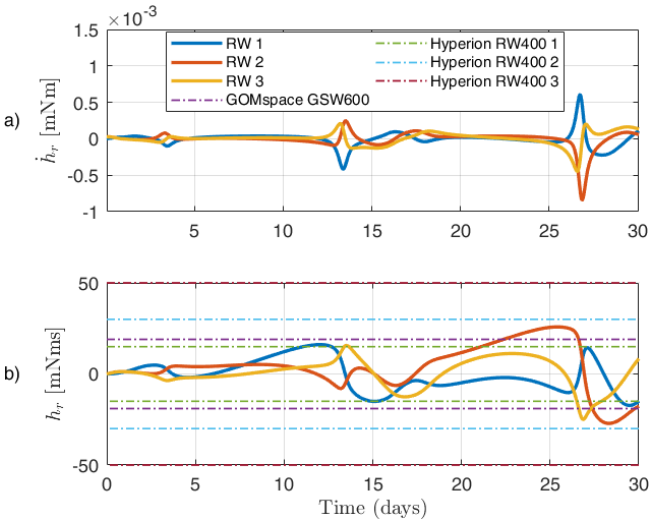

Fig. 8: a) Torque and b) angular momentum for the 60° tetrahedron RWs configuration during the first 30 days in the operational orbit.

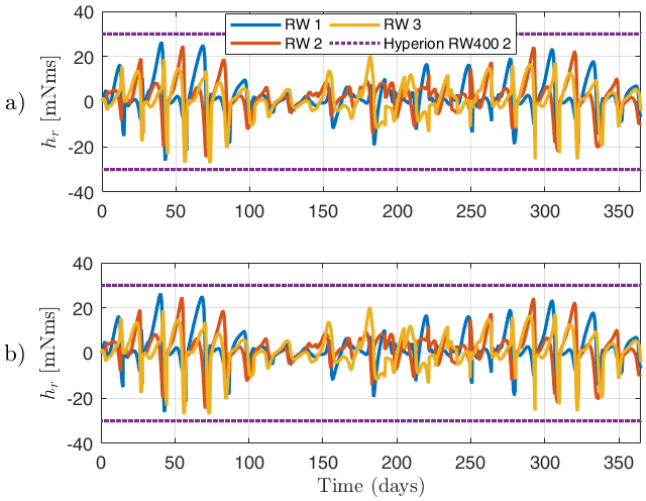

Fig. 9: Angular momentum evolution for a rigid desaturation schedule employing a) projective thrusters control, and b) optimal thrusters control.

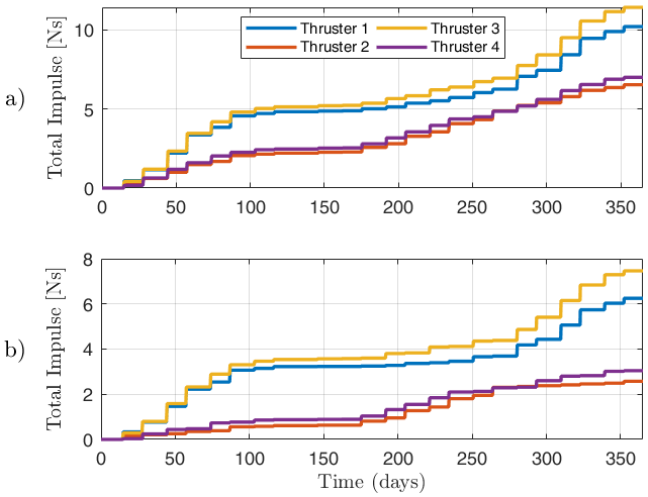

Fig. 11: Thrusters impulse evolution for a rigid desaturation schedule employing a) projective thrusters control, and b) optimal thrusters control.

operating at a fixed thrust level. A maximum torque of 0.25 mNm and angular velocity of 2×10^{-4} rad/s was produced with this configuration, satisfying both the torque capabilities of the RWs and the requirement ADCS-05. The optimal thrusters control is compared with the previous by placing the same parameters with a larger $k_3 = 0.3$, which according to Eq. (21) results in a faster desaturation. The maximum torque for this simulation is 7 mNm with a maximum angular velocity of 3×10^{-4} rad/s, satisfying again the torque capabilities of the RWs and the requirement ADCS-05. This time, however, the increase in k_3 brings the maximum torque closer to the limit of the RWs.

Angular momentum, pointing angle, total impulse and parasitic ΔV plots are given in Figs. 9, 10, 11 and 12, respectively. The saturation limits are always respected, but an off-pointing of up to 0.2°, slightly larger than the 0.1° limit imposed by the requirement ADCS-03, is produced in some maneuvers. The steeper desaturation control law of the optimal thrusters control scenario increases the off-pointing in most cases. In terms of performance, the optimal control achieves a significantly lower propellant consumption with total impulse reductions of a 45% with respect to the projective control. This implies a significantly lower parasitic ΔV, which is mainly directed in the X axis.

5.3 Flexible desaturation schedule

In the flexible desaturation scheme, the desaturation routine is activated when 90% of the maximum momentum is reached and stopped when a 66% is achieved. In this way, the previously observed oscillatory angular momentum evolution of the reaction wheels are employed to save propellant. The

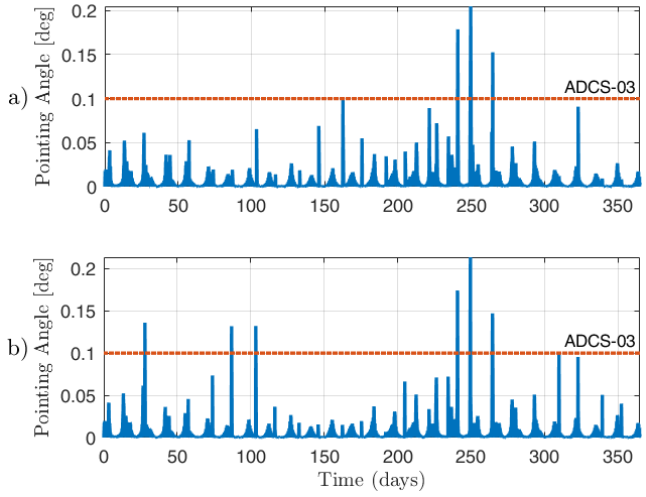

Fig. 10: Pointing angle evolution for a rigid desaturation schedule employing a) projective thrusters control, and b) optimal thrusters control.

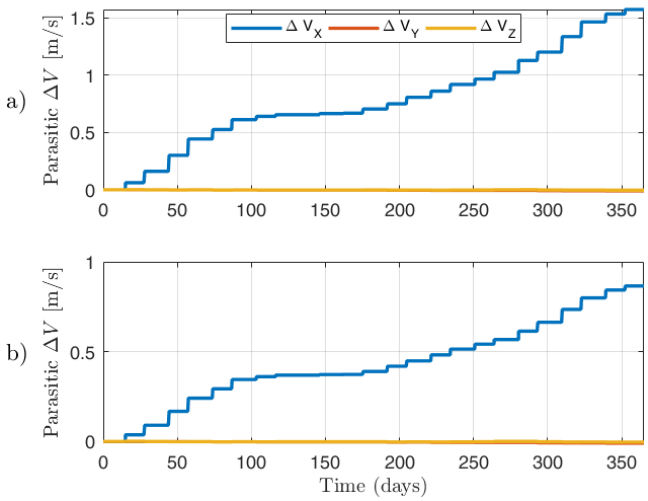

Fig. 12: Parasitic ΔV evolution for a rigid desaturation schedule employing a) projective thrusters control, and b) optimal thrusters control.

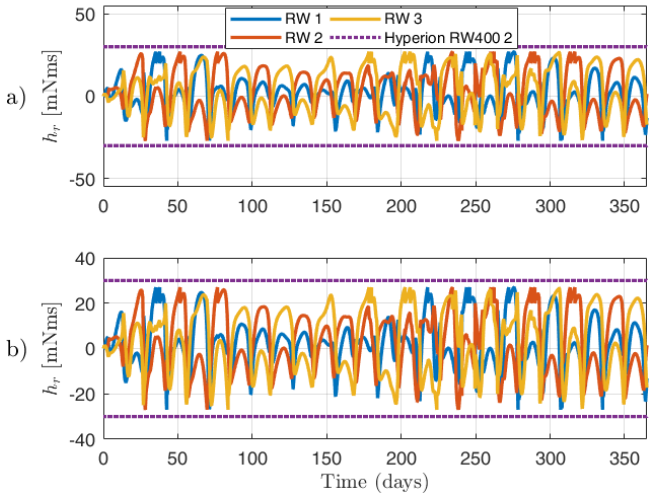

Fig. 13: Angular momentum evolution for a flexible desaturation schedule employing a) projective thrusters control, and b) optimal thrusters control.

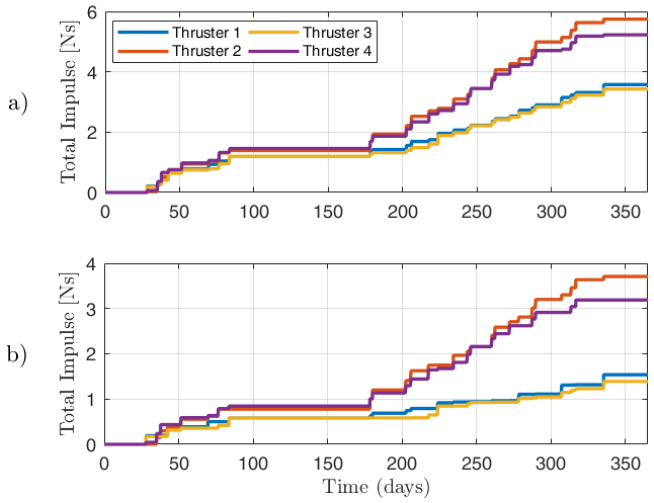

Fig. 15: Thrusters impulse evolution for a flexible desaturation schedule employing a) projective thrusters control, and b) optimal thrusters control.

activation and stopping thresholds have been chosen arbitrarily, and indeed power consumption may be reduced with lower values.

The control parameters are set to $k_1 = 0.0005$, $k_2 = 0.0005$, $k_3 = 0.0005$ and $k_4 = 0.5$ for the projective thrusters control case. As before, $k_1 = 100$ and $k_2 = 100$ during desaturation. The maximum simulated torque is 0.15 mNm, while the angular velocity reached 2×10^{-4} rad/s. These values satisfy again the torque capabilities of the RWs and the requirement ADCS-05. The optimal thrusters control parameters are the same but implementing a more demanding RWs desaturation law with $k_3 = 0.3$. A maximum torque of 8 mNm and angular velocity of 4×10^{-4} rad/s was produced with this configuration, saturating the RWs and failing the requirement ADCS-05 on a single maneuver.

Angular momentum, pointing angle, total impulse and parasitic ΔV plots are depicted for the new desaturation strategy in Figs. 13, 14, 15 and 16, respectively. As in the rigid desaturation case, the saturation limits are always respected, but an off-pointing of up to 0.2° is again produced in some maneuvers and becomes slightly larger when k_3 acquires a larger value. A lower propellant consumption is observed with the optimal control, achieving total impulse and parasitic ΔV reductions of a 45% with respect to the projective control.

5.4 Summary of desaturation results

The main outputs of the previously discussed desaturation strategies have been summarized in Tab. 6. Although no attempt was made to optimize the set of parameters k_i, the flexible-optimal desaturation arises as the most efficient in

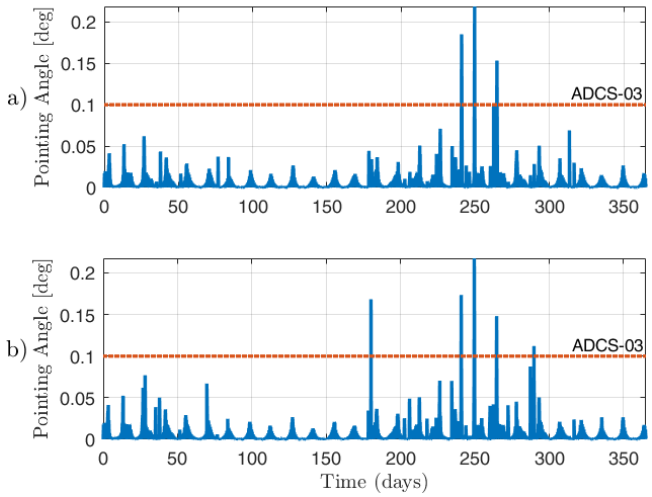

Fig. 14: Pointing angle evolution for a flexible desaturation schedule employing a) projective thrusters control, and b) optimal thrusters control.

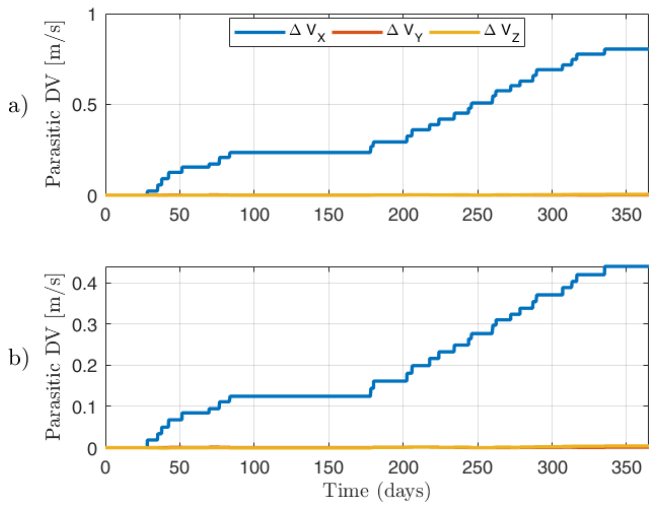

Fig. 16: Parasitic ΔV evolution for a flexible desaturation schedule employing a) projective thrusters control, and b) optimal thrusters control.

Tab. 6: Summary of performances for different desaturation strategies and a 1-year mission.

	Rigid Proj.	**Rigid Opt.**	**Flex. Proj.**	**Flex. Opt.**
$\mathbf{k_1}$	$5 \cdot 10^{-4}$	$5 \cdot 10^{-4}$	$5 \cdot 10^{-4}$	$5 \cdot 10^{-4}$
$\mathbf{k_2}$	$5 \cdot 10^{-4}$	$5 \cdot 10^{-4}$	$5 \cdot 10^{-4}$	$5 \cdot 10^{-4}$
$\mathbf{k_1^{des}}$	100	100	100	100
$\mathbf{k_2^{des}}$	100	100	100	100
$\mathbf{k_3}$	0.01	0.3	$5 \cdot 10^{-4}$	$5 \cdot 10^{-4}$
$\mathbf{k_4}$	0.5	0.5	0.5	0.5
T.I. (Ns)	35.134	19.333	17.973	9.822
ΔV (m/s)	1.573	0.865	0.805	0.440

terms of propellant consumption. In all cases, the parasitic ΔV is shown to be negligible in comparison with the station-keeping ΔV, which for LUMIO's orbit was estimated to be 18.3 m/s with a 1σ interval.

6 Conclusions and future work

The post-CDR ADCS design of LUMIO has been presented in this paper. Suitable RW models and configurations are analyzed with the goal of extending the time period between desaturation maneuvers. A desaturation strategy is developed on which the off-pointing of the satellite is not necessarily produced, and various numerical implementations are tested.

A set of three Hyperion RW400 2 (maximum angular momentum of 30 mNms, maximum torque of 8 mNm) is selected and oriented in a 60° tetrahedron configuration. The simulations, based on a simplified SRP model, show that this setup is able to remain more than 15 days without reaching saturation. Mass savings of 510 grams are achieved with respect to the baseline configuration.

Among the desaturation strategies under study, the flexible schedule with an optimal thrusters control law is identified as the most efficient in terms of propellant consumption. The feasibility of this implementation relies on the throttlability of the Aerojet MPS-130 ADCS thrusters and the proper selection of the control parameters k_i. Although less efficient, a projective control could also be used if a single thrust value is generated by each thruster. In all cases the parasitic ΔV is shown to be negligible in comparison with the station-keeping costraint.

The ADCS requirements listed in Tab. 3 were generally satisfied by the proposed configuration. Only small deviations in the pointing angle (ADCS-03) were observed for certain maneuvers, but these are due to a mismatch between the torque produced by the ADCS thrusters and the RWs during desaturation. A proper tuning of the k_i parameters should then be able to overcome this problem.

This study was not aimed to optimize the configuration and control parameters of the system. Small differences in performance are observed between the proposed RW arrangements, and hence the selected 60° tetrahedron has to be taken just as a suitable solution. Future works should address the effect of different configurations on power consumption and angular momentum storage by making use, for instance, of the procedure described in [18]. The desaturation strategy and control parameters k_i should be selected to satisfy further mission requirements in next phases of development. Those may include the minimization of power and energy consumption, the avoidance of structural and liquid sloshing resonance frequencies or other operational restrictions.

Acknowledgments

The work described in this paper is a spin-off of a bigger project: LUMIO. For this reason the authors are grateful to the whole LUMIO Team. The authors would like to acknowledge fruitful discussions with Simone Ceccherini and Palash Patole, which were greatly appreciated.

Appendix A: Stability proofs

The desaturation law described by Eq. (20) (RW, tracking), Eq. (21) (RW, desaturation) and Eq. (22) (thrusters, tracking) result in asymptotically stable dynamics if (a) the spacecraft is driven to the desired attitude during normal operation, (b) the reaction wheels reach the desired state $\vec{h}_r^d$ during desaturation, and (c) the spacecraft keeps the desired attitude during desaturation.

According to the Lyapunov's Second Stability Theorem, an autonomous nonlinear dynamic system described by [19]

$$\dot{\vec{x}} = f(\vec{x}), \quad f(\vec{x}^e) = 0, \tag{24}$$

where $\vec{x}^e$ is an isolated equilibrium point, is said to be asymptotically stable if in some finite neighbourhood D of $\vec{x}^e$ there exists a scalar function $V(\vec{x})$ with continuous first partial derivatives in $\vec{x}$ and t that satisfies

$$\text{(i) } V(\vec{x}) > 0 \text{ for all } \vec{x} \neq \vec{x}^* \text{ in } D \text{ and } V(\vec{x}^*) = 0, \tag{25}$$

$$\text{(ii) } \dot{V}(\vec{x}) < 0 \text{ for all } \vec{x} \neq \vec{x}^* \text{ in } D \text{ and } \dot{V}(\vec{x}^*) = 0. \tag{26}$$

For the aforementioned case (a), the Lyapunov function

$$V(\vec{x}) = \frac{1}{2}\vec{\omega}_e J \vec{\omega}_e + k_2 tr(I - A_e) \tag{27}$$

can be differentiated to give

$$\dot{V}(\vec{x}) = \vec{\omega}_e J \dot{\vec{\omega}}_e - k_2 tr(\dot{A}_e). \tag{28}$$

Implementing the DCM Kinematic Differential Equation $\dot{A}_e = -\vec{\omega}_e^V A_e$ and considering that

$$\begin{aligned} \dot{\vec{\omega}}_e &= \dot{\vec{\omega}} - \frac{\mathrm{d}}{\mathrm{d}t}\left(A_e \vec{\omega}_d\right) \\ &= J^{-1}(J\vec{\omega} \times \vec{\omega} + \vec{u} + \vec{d}) - \frac{\mathrm{d}}{\mathrm{d}t}\left(A_e \vec{\omega}_d\right) \end{aligned} \tag{29}$$

then the derivative of the Lyapunov function given in Eq. (27) results

$$\dot{V}(\vec{x}) = \vec{\omega}_e \left[J\vec{\omega} \times \vec{\omega} + \vec{u} + \hat{\vec{d}} - J\frac{\mathrm{d}}{\mathrm{d}t}\left(A_e \vec{\omega}_d\right) - k_2 (A_e - A_e^T)^V \right], \tag{30}$$

where the property $tr(\vec{\omega}_e^{\times} A_e) = -\vec{\omega}_e^T (A_e - A_e^T)^V$ has been used. If the control law represented by Eq. (20) is substituted, the result is

$$\dot{V}(\vec{x}) = -k_1 w_e^2 \tag{31}$$

and hence the conditions given by Eq. (26) and Eq. (26) are satisfied. In other words, the tracking control law makes the system asymptotically stable.

For the case (b), the stability condition is demonstrated by substituting Eq. (21) into Eq. (12), which gives

$$\dot{\vec{h}}_r = -k_3(\vec{h}_r - \text{sign}(\vec{h}_r^T) \odot \vec{h}_r^d). \tag{32}$$

This is a first-order differential equation whose solution asymptotically tends to the desired values $\vec{h}_r^d$.

Finally, the procedure described in case (a) can be used to demonstrate that the control law in case (c) asymptotically stabilizes the system. This time, the disturbance vector includes a new term $-\vec{u}_c$, that arises from the desaturation torque of the reaction wheels.

References

[1] E. Hand. "Interplanetary small satellites come of age". In: *Science* 361.6404 (2018), pp. 736–737.

[2] A. Klesh, B. Clement, C. Colley, J. Essmiller, D. Forgette, J. Krajewski, A. Marinan, T. Martin-Mur, J. Steinkraus, D. Sternberg, T. Werne, and B. Young. "MarCO: Early Operations of the First CubeSats to Mars". In: *Proceedings of the AIAA/USU Conference on Small Satellites. Session 9*. 2018.

[3] H. Heidt, J. Puig-Suari, A. S. Moore, S. Nakasuka, and R. J. Twiggs. "CubeSat: A new Generation of Picosatellite for Education and Industry Low-Cost Space Experimentation". In: *Proceedings of the AIAA/USU Conference on Small Satellites. Session 5*. 2000.

[4] G. Benedetti, N. Bloise, D. Boi, F. Caruso, A. Civita, S. Corpino, E. Garofalo, G. Governale, L. Mascolo, G. Mazzella, M. Quarata, D. Riccobono, G. Sacchiero, D. Teodonio, and P. M. Vernicari. "Interplanetary CubeSats for asteroid exploration: Mission analysis and design". In: *Acta Astronautica* 154 (2019), pp. 238–255.

[5] A. Schorr, K. F. Robinson, and D. Hitt. "NASA's Space Launch System: Enabling Exploration and Discovery". In: *Proceedings of the 15th Reinventing Space Conference. BIS-RS-2017-13*. Oct. 1, 2017.

[6] S. Speretta, A. Cervone, P. Sundaramoorthy, R. Noomen, S. Mestry, A. Cipriano, F. Topputo, J. Biggs, P. Di Lizia, M. Massari, K. V. Mani, D. A. Dei Tos, S. Ceccherini, V. Franzese, A. Ivanov, D. Labate, L. Tommasi, A. Jochemsen, J. Gailis, R. Furfaro, V. Reddy, J. Vennekens, and R. Walker. "LUMIO: An Autonomous CubeSat for Lunar Exploration". In: *Space Operations: Inspiring Humankind's Future*. Ed. by H. Pasquier, C. A. Cruzen, M. Schmidhuber, and Y. H. Lee. Cham: Springer International Publishing, 2019, pp. 103–134.

[7] F. Topputo, M. Massari, J. Biggs, P. Di Lizia, D. Dei Tos, K. Mani, S. Ceccherini, V. Franzese, A. Cervone, R. Noomen, P. Sundaramoorthy, S. Speretta, S. Mestry, A. Carmo Cipriano, S. Pepper, M. van de Poel, A. Ivanov, D. Labate, L. Tommasi, A. Jochemsen, Q. Leroy, R. Furfaro, V. Reddy, and K. Jacquinot. *Lunar Meteoroid Impact Observer: a CubeSat at Earth-Moon L2*. European Space Agency, Nov. 1, 2017.

[8] V. Franzese, P. Di Lizia, and F. Topputo. "Autonomous Optical Navigation for the Lunar Meteoroid Impacts Observer". In: *Journal of Guidance, Control, and Dynamics* 42.7 (2019), pp. 1579–1586.

[9] ESA-ESTEC. *CDF Study Report of Lunar Meteoroid Impacts Observer (LUMIO) Mission*. Tech. rep. LUMIO-CDF-R-36. European Space Agency, Noordwijk, the Netherlands, May 2018.

[10] European Space Agency. *CDF Study Report of LUMIO: Review of SysNova Award LUMIO Study*. European Space Agency, Feb. 1, 2018.

[11] Ana Cipriano, Diogene Alessandro Dei Tos, and Francesco Topputo. "Orbit Design for LUMIO: The Lunar Meteoroid Impacts Observer". In: *Frontiers in Astronomy and Space Sciences* 5 (2018), pp. 1–23.

[12] R. Floberghagen, P. Visser, and F. Weischede. "Lunar Albedo Force Modeling and its Effect on Low Lunar Orbit and Gravity Field Determination". In: *Advances in Space Research* 23.4 (1999), pp. 733–788.

[13] B. Wie. *Space Vehicle Dynamics and Control*. AIAA Education Series, 2006.

[14] S. Abolfazl and M. Mehran. In: *International Journal of Aeronautical and Space Sciences* 15.2 (2014), pp. 190–198.

[15] H. Kurokawa. "A Geometric Study of Single Gimbal Control Moment Gyros". In: 1998.

[16] T. Shengyong, C. Xibin, and Z. Yulin. "Configuration optimization of four dissimilar redundant flywheels with application to IPACS". In: *Proceedings of the 31st Chinese Control Conference*. 2012, pp. 4664–4669.

[17] Z. Ismail and R. Varatharajoo. "A study of reaction wheel configurations for a 3-axis satellite attitude control". In: *Advances in Space Research* 45.6 (2010), pp. 750–759.

[18] D. S. Bayard. "An optimization result with application to optimal spacecraft reaction wheel orientation design". In: *Proceedings of the 2001 American Control Conference. (Cat. No.01CH37148)*. Vol. 2. 2001, 1473–1478 vol.2.

[19] H. Schaub and J. L. Junkins. *Analytical Mechanics of Space Systems*. American Institute of Aeronautics and Astronautics (AIAA), 2003.

[20] D. Schmuland, C. Carpenter, R. Masse, and J. Overly. "New insights into additive manufacturing processes: enabling low-cost, high-impulse propulsion systems". In: *Proceedings of the 27th Annual AIAA/USU Conference on Small Satellites* (2013).

[21] R. S. Sanchez Pena, R. Alonso, and P. A. Anigstein. "Robust optimal solution to the attitude/force control problem". In: *IEEE Transactions on Aerospace and Electronic Systems* 36.3 (2000), pp. 784–792.

[22] Y. Bai, J. D. Biggs, X. Wang, and N. Cui. "A singular adaptive attitude control with active disturbance rejection". In: *European Journal of Control* 35 (2017), pp. 50–56.

[23] Y. Bai, J. D. Biggs, F. Bernelli-Zazzera, and N. Cui. "Adaptive Attitude Tracking with Active Uncertainty Rejection". In: *Journal of Guidance, Control, and Dynamics* 41.2 (2018), pp. 550–558.